A full-dimensional multilayer multiconfiguration time-dependent Hartree study on the ultraviolet absorption spectrum of formaldehyde oxide

Qingyong Meng and Hans-Dieter Meyer

Articles you may be interested in

Full-dimensional multilayer multiconfigurational time-dependent Hartree study of electron transfer dynamics in the anthracene/C60 complex
J. Chem. Phys. **142**, 084706 (2015); 10.1063/1.4909521

A time-dependent density-functional theory and complete active space self-consistent field method study of vibronic absorption and emission spectra of coumarin
J. Chem. Phys. **141**, 014306 (2014); 10.1063/1.4885845

A multilayer MCTDH study on the full dimensional vibronic dynamics of naphthalene and anthracene cations
J. Chem. Phys. **138**, 014313 (2013); 10.1063/1.4772779

Full dimensional quantum-mechanical simulations for the vibronic dynamics of difluorobenzene radical cation isomers using the multilayer multiconfiguration time-dependent Hartree method
J. Chem. Phys. **137**, 134302 (2012); 10.1063/1.4755372

Multimode quantum dynamics using Gaussian wavepackets: The Gaussian-based multiconfiguration time-dependent Hartree (G-MCTDH) method applied to the absorption spectrum of pyrazine
J. Chem. Phys. **129**, 174104 (2008); 10.1063/1.2996349

A full-dimensional multilayer multiconfiguration time-dependent Hartree study on the ultraviolet absorption spectrum of formaldehyde oxide

Qingyong Meng[1,a)] and Hans-Dieter Meyer[2,b)]

[1]*State Key Laboratory of Molecular Reaction Dynamics, Dalian Institute of Chemical Physics, Chinese Academy of Sciences, Zhongshan Road 457, 116023 Dalian, China*
[2]*Theoretische Chemie, Physikalisch-Chemisches Institut, Ruprecht-Karls Universität Heidelberg, Im Neuenheimer Feld 229, D-69120 Heidelberg, Germany*

Employing the multilayer multiconfiguration time-dependent Hartree (ML-MCTDH) method in conjunction with the multistate multimode vibronic coupling Hamiltonian (MMVCH) model, we perform a full dimensional (9D) quantum dynamical study on the simplest Criegee intermediate, formaldehyde oxide, in five lower-lying singlet electronic states. The ultraviolet (UV) spectrum is then simulated by a Fourier transform of the auto-correlation function. The MMVCH model is built based on extensive MRCI(8e,8o)/aug-cc-pVTZ calculations. To ensure a fast convergence of the final calculations, a large number of ML-MCTDH test calculations is performed to find an appropriate multilayer separations (ML-trees) of the ML-MCTDH nuclear wave functions, and the dynamical calculations are carefully checked to ensure that the calculations are well converged. To compare the computational efficiency, standard MCTDH simulations using the same Hamiltonian are also performed. A comparison of the MCTDH and ML-MCTDH calculations shows that even for the present not-too-large system (9D here) the ML-MCTDH calculations can save a considerable amount of computational resources while producing identical spectra as the MCTDH calculations. Furthermore, the present theoretical $\tilde{B}\,^1A' \leftarrow \tilde{X}\,^1A'$ UV spectral band and the corresponding experimental measurements [J. M. Beames, F. Liu, L. Lu, and M. I. Lester, J. Am. Chem. Soc. **134**, 20045–20048 (2012); L. Sheps, J. Phys. Chem. Lett. **4**, 4201–4205 (2013); W.-L. Ting, Y.-H. Chen, W. Chao, M. C. Smith, and J. J.-M. Lin, Phys. Chem. Chem. Phys. **16**, 10438–10443 (2014)] are discussed. To the best of our knowledge, this is the first theoretical UV spectrum simulated for this molecule including nuclear motion beyond an adiabatic harmonic approximation. © *2014 AIP Publishing LLC*. [http://dx.doi.org/10.1063/1.4896201]

I. INTRODUCTION

Despite its importance in ozonolysis of alkenes, the direct detection of the simplest Criegee intermediates, formaldehyde oxide (CH_2OO), was not reported until recently.[1–3] Since then, extensive studies[4–17] on formaldehyde oxide were reported in the literature. Besides as an intermediate in ozonolysis of alkenes, formaldehyde oxide was also considered as an important intermediates in forming atmospheric SO_3, OH, and NO_3,[7,11–14] which may play a key role in aerosol and cloud formation. Moreover, formaldehyde oxide can be photolyzed by near ultraviolet (UV) light to form O (^1D_g),[9,17] which is an important species in atmospheric reaction.

To detect formaldehyde oxide in a reaction system, the spectra of formaldehyde oxide were reported by theoretical simulations[6] and experimental measurements in both UV[5,9,10,16] and infrared (IR)[17,18] regions. In 2012, Lee *et al.*[6] reported the simulated electronic spectrum for the $\tilde{B}\,^1A' \leftarrow \tilde{X}\,^1A'$ transition using high level time-independent electronic-structure calculations, including RCCSD(T), CASSCF//NEVPT2, and CASSCF//MRCI+D

methods. On the basis of these calculations, they[6] predict two peaks at ∼5.17 and ∼4.59 eV (i.e., ∼240 and ∼270 nm, respectively) in the spectrum of $\tilde{B}$ band. In 2012, Beames *et al.*[5] reported a strong UV spectrum band for the $\tilde{B}\,^1A' \leftarrow \tilde{X}\,^1A'$ transition in the 3.54 ∼ 3.87 eV (320 ∼ 350 nm) region. In 2013, Sheps[10] measured the UV absorption $\tilde{B}$ band, where formaldehyde oxide was produced by the reaction of CH_2I radicals with O_2. In contrast to the spectrum reported by Beames *et al.*,[5] this spectrum[10] extends to longer wavelengths and exhibits resolved vibrational structure on its low-energy side. Recently, Ting *et al.*[16] reported their UV absorption cross sections of the $\tilde{B}$ band, in which SO_2 scavenging and self-reaction of CH_2OO were utilized for the decay of CH_2OO to extract the absorption spectrum under bulk conditions.

From a technical point of view, the multiconfiguration time-dependent Hartree (MCTDH)[19–25] and multilayer MCTDH (ML-MCTDH)[26–28] methods have become important tools to accurately describe the quantum dynamics of complex multidimensional systems. As discussed by Vendrell and Meyer[28] using 6D, 18D, and 1458D Henon-Heiles (HH) model Hamiltonians, for the 6D case the MCTDH simulation is more efficient than the corresponding ML-MCTDH one, while the 18D ML-MCTDH simulation outperforms

a)Electronic mail: mengqingyong@dicp.ac.cn
b)Electronic mail: hans-dieter.meyer@pci.uni-heidelberg.de

the corresponding MCTDH calculation. For the 1458D case only ML-MCTDH calculations were possible. It was then concluded that the calculation efficiencies of MCTDH and ML-MCTDH may become similar for the systems with the dimensionality of ~10. In the present work, as formaldehyde oxide has nine nuclear degrees of freedom (DOFs), it is possible to perform the full dimensional quantum dynamics calculations by using both the MCTDH[19–25] and ML-MCTDH[26–28] methods. Furthermore, it is an appropriate model to determine whether the ML-MCTDH is still more efficient than MCTDH in the case of ~10D.

In the present work, based on the high-level multireference configuration interaction (MRCI)[29–35] for building the multistate multimode vibronic coupling Hamiltonian (MMVCH)[36,37] model, the full dimensional MCTDH[19–25] and ML-MCTDH[26–28] calculations are performed to simulate the UV spectrum. Here the nuclear DOFs are coupled and the Hamiltonian necessarily goes beyond the adiabatic Born-Oppenheimer framework, since a coupling between electronic and nuclear DOFs leads to nonadiabaticity. Our efforts are driven by the desire to understand the underlying broad vibronic bands of the excited electronic states, in particular the $\tilde{B}\,^1A'$ state of formaldehyde oxide. This state is considered as the only bright state among the four lower-lying singlet excited states (below ~8.0 eV).[6]

This paper is organized as follows. In Sec. II, we will briefly describe the computational details for the present approach. Section III presents the spectra of formaldehyde oxide, and a discussion on previous spectra of this system. Finally, Sec. IV concludes with a summary.

II. COMPUTATIONAL DETAILS

Geometry and atom labellings of the formaldehyde oxide molecule is shown in Figure 1. Here $R(O_1 - O_2)$, $R(C - O_1)$, and $R(C - H_2)$ are bond lengths of $O_1 - O_2$, $C - O_1$, and $C - H_2$, respectively, while $A(H_1CH_2)$ and $A(CO_1O_2)$ are bond angles. Since the $C - H_1$ bond length is only ~0.003 Å larger than the $C - H_2$ bond length, we shall only report the $R(C - H_2)$ values in Sec. III. Similarly, since the $H_1 - C - O_1$ bond angle is ~3° larger than the $H_2 - C - O_1$ angle, only $A(H_1CH_2)$ values are given in the following text.
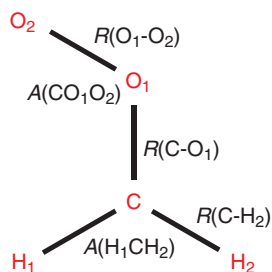

FIG. 1. Geometry and atom labellings of formaldehyde oxide in the C_s point group used in the present work. Here $R(O_1 - O_2)$, $R(C - O_1)$, and $R(C - H_2)$ denote the bond lengths of the $O_1 - O_2$, $C - O_1$, and $C - H_2$ bonds, respectively. $A(H_1CH_2)$ and $A(CO_1O_2)$ denote the bond angles. Finally, the dihedral angles between the OCO and HCH planes is 0.0°.

A. The Hamiltonian model

To study the vibronic dynamics of the electronic states and to avoid singular non-adiabatic coupling among these states, we adopt a diabatic electronic basis. An MMVCH model[36,37] pertaining to this situation is given by $\mathbf{H} = (T_N + V_0)\mathbf{1} + \mathbf{W}$, where $T_N + V_0$ represents the sum of the harmonic vibrational energies of all modes, namely

$$T_N + V_0 = \frac{1}{2}\sum_i \omega_i \left(-\partial_i^2 + q_i^2\right). \tag{1}$$

We use mass- and frequency-scaled, and hence dimensionless, normal mode coordinates, where ω_i denotes the ground-state vibrational frequency of the ith normal mode (denoted as q_i). The elements of the $\mathbf{W}$ matrix are expanded as a Taylor series in q_i around the Frank-Condon point. In the present work, the linear and quadratic terms for the diagonal elements W_{JJ} and linear terms for the off-diagonal elements W_{JK} are retained, namely[36–38]

$$
\begin{aligned}
W_{JJ} &= E_v^{(J)} + \sum_{i \in A'} \kappa_i^{(J)} q_i + \frac{1}{2}\sum_{i \in A'} \gamma_i^{(J)} q_i^2, \\
W_{JK} &= \sum_{i \in \Gamma_J \otimes \Gamma_K} \lambda_i^{(J,K)} q_i.
\end{aligned}
\tag{2}
$$

Here $E_v^{(J)}$ denotes the vertical excitation energy (E_v) of the Jth electronic state. The intra-state linear couplings $\kappa_i^{(J)}$ and quadratic couplings $\gamma_i^{(J)}$ represent the gradient and curvature along the totally symmetric vibrational modes, respectively, where the derivative is to be taken at the Frank-Condon zone center $\mathbf{q} = \mathbf{0}$.[36,37] The inter-state linear couplings $\lambda_i^{(J,K)}$ in Eq. (2) represent the coupling parameters between the electronic states J and K accomplished through the ith mode. This mode must satisfy the selection rule $\Gamma_J \otimes \Gamma_i \otimes \Gamma_K \supset A'$, where Γ represents the irreducible representation of the electronic state or vibrational mode, otherwise the coupling vanishes.[36,37] We refer readers to Refs. 36 and 37 for details of the present MMVCH model.

In the present work, the ground-state geometry is optimized at the CASSCF and MRCI levels. Then the CASSCF vibrational analysis is performed to obtain the ground-state vibrational frequencies and the normal mode coordinates. Since there is no analytic gradient for the MRCI energy, the various parameters entering the Hamiltonian are then calculated using finite displacements along the potential energy functions of the various normal coordinates at the MRCI level.

All CASSCF and MRCI calculations[29–35] are carried out using MOLPRO version 2012.1.[39,40] The augmented Dunning's correlation consistent polarized valence triple zeta (aug-cc-pVTZ or aVTZ)[41–47] basis set is used. With a quadratically convergent multiconfiguration SCF (MCSCF)[30,31] wave function constituting the reference function, the internally contracted multireference CISD (ic-MRCISD)[29,32–35] calculations are performed to compute the MRCI wave function and energy in the active space. For calculating the MMVCH models of formaldehyde oxide, 8 electrons and 8 orbitals (i.e., (8e, 8o) space) are active, same as in the

previous theoretical studies.[48] Here, the $\sigma(CO)$, the $\sigma(OO)$, the two π orbitals, and the corresponding anti-bonding orbitals, i.e., 4 orbitals of a' and 4 orbitals of a'' symmetry, are included in the (8e,8o) active space. Convergence of this smaller active space is checked by comparison with the corresponding E_v values calculated from the full valence active space (14e,12o).

B. The MCTDH and ML-MCTDH simulations

A wave packet propagation approach within the multilayer multiconfiguration time-dependent Hartree (ML-MCTDH) scheme[26–28] employed here appears to be the best choice in this full dimensional dynamics simulation. The ML-MCTDH calculations for wave-packet propagation are carried out using the Heidelberg MCTDH package.[49] In the ML-MCTDH scheme,[26–28] the nuclear wave-function is written as a layered structure and the SPFs of combined DOFs are expanded in MCTDH form, that is in the form[26–28]

$$\varphi_m^{z-1;\kappa_{l-1}}\left(Q_{\kappa_{l-1}}^{z-1},t\right) = \sum_{j_1}^{n_1} \cdots \sum_{j_{p_{\kappa_l}}}^{n_{\kappa_l}} A_{m;j_1,\ldots,j_{p_{\kappa_l}}}^{z}(t) \prod_{\kappa_l=1}^{p_{\kappa_l}} \varphi_{j_{\kappa_l}}^{z,\kappa_l}\left(Q_{\kappa_l}^{z}\right)$$

$$= \sum_J A_{m;J}^{z} \cdot \Phi_J^{z}\left(Q_{\kappa_l}^{z}\right), \qquad (3)$$

where $z = \{l; \kappa_1,\ldots,\kappa_{l-1}\}$ and $z - 1 = \{l - 1; \kappa_1,\ldots, \kappa_{l-2}\}$, l denotes the layer depth, and $Q_{\kappa_{l-1}}^{z-1}$ is a combination of logical coordinates with $Q_{\kappa_{l-1}}^{z-1} = \{Q_1^z,\ldots,Q_{p_{\kappa_l}}^z\}$. The logical coordinate is a combination scheme of several vibrational modes q_i. The SPFs of the last layer are expanded in time-independent primitive basis functions (in practice Discrete Variable Representation (DVR)[50,51] grids). Note that the MCTDH scheme is a special case of ML-MCTDH with $l = 2$.[28] Based on this layered wave function (3), the equations of motion[26–28] are then deduced using the Dirac-Frenkel variational principle.

Assuming broadband instantaneous excitation, the molecule is initially in one of the electronic states and the initial wave packets in each electronic states are propagated individually. Furthermore, assuming the Condon approximation, we take the initial state $|\Psi(0)\rangle$ to be the ground state harmonic oscillator wave packet, located on one of the diabatic potential energy surfaces (PESs) at the centre of the Frank-Condon zone. To compute the spectrum, we evaluate the autocorrelation function $C(t) = \langle\Psi(0)|\Psi(t)\rangle$. The Fourier transform of $C(t)$ is then performed to yield the corresponding spectrum.[22,36,38,52]

A tree diagram (ML-tree) is drawn in Figure 2 to illustrate the structure of the ML-MCTDH wave function.[27,28] In order to achieve a fast and stable convergence, the ML-tree need to be designed carefully and optimized iteratively based on the coupling intensities among the ML-tree nodes which are expressed by the node populations.[27,28,53,54] The ML-trees optimized for the present work are given in Figure 2 together with numbers of SPFs for the modes of each layer. The numerical detail of the ML-MCTDH calculations, including the size of primitive basis and mode-combination scheme, are also given in ML-trees.

All of the dynamics simulations are carried out on the same machine and CPU type (Intel® Xeon® CPU E5520, 2261 MHz) using a single core. The integration schemes variable mean field (VMF) and constant mean field (CMF)[22,55] are used for ML-MCTDH and MCTDH calculations, respectively.

III. RESULTS AND DISCUSSION

A. The multistate multimode vibronic coupling Hamiltonian

As a basis for the subsequent dynamical calculations, we start here with the key quantities of the present Hamiltonian model. The symmetry assignments and vertical excitation energies E_v (based on the corresponding theoretical equilibrium geometry) of formaldehyde oxide are given in Table I. Given in Table II are the present and the previously reported theoretical geometries[18,48,56,57] of the ground state.

In the present work, four singlet electronic excited-states of formaldehyde oxide: $1\,^1A''$, $2\,^1A'$, $3\,^1A'$, and $2\,^1A''$ are involved in the Hamiltonian. As given in Sec. II, all parameters appearing in the **W** matrix, including the vertical excitation energies $E_v^{(J)}$, coupling constants $\kappa_i^{(J)}$, $\lambda_i^{(J,K)}$, and $g_i^{(J)}$ are calculated at the MRCI/aVTZ level. Before discussing the simulated spectra, let us first inspect the results on the electronic states of formaldehyde oxide.

1. Electronic states

At the corresponding optimized geometries of the ground-state formaldehyde oxide, the MRCI and CASSCF energy calculations for the lower-lying singlet and triplet states predict the E_v values of formaldehyde oxide as given in Table I. In order to check the convergence of the present (8e,8o) active space, these E_v values are also calculated by using MRCI and CASSCF methods with a full valence active space (14e,12o). All of these E_v values, together with the previously reported values[6] are also given in Table I.

The MRCI calculations predict the E_v values (given in parentheses are MRCI(14e,12o) E_v values) of 1.87 (1.81), 2.65 (2.48), 2.70 (2.57), 3.89 (4.03), 6.82 (6.96), and 7.08 (7.01) eV for $1\,^3A'$, $1\,^3A''$, $1\,^1A''$, $2\,^1A'$, $3\,^1A'$, and $2\,^1A''$, respectively. For each electronic states, the differences between MRCI(8e,8o) and MRCI(14e,12o) E_v values are smaller than 0.17 eV. Similarly, as shown in Table I, except for $2\,^1A''$ the differences between CASSCF(8e,8o) and CASSCF(14e,12o) E_v values are smaller than 0.15 eV. In addition, for $2\,^1A'$, the present MRCI(8e,8o) E_v value (3.89 eV) is 0.04 eV smaller than the previous MRCI(12e,11o) value (3.93 eV).[6] The fact that the MRCI(8e,8o) results are very close to the corresponding MRCI(14e,12o) results indicates that the (8e,8o) active space is appropriate to build the MMVCH model. Having discussed the convergence of the active space, let us turn to the E_v values themselves. From the MRCI E_v calculations, one can denote $1\,^1A'$, $1\,^1A''$, $2\,^1A'$, $3\,^1A'$, and $2\,^1A''$ as $\tilde{X}$, $\tilde{A}$, $\tilde{B}$, $\tilde{C}$, and $\tilde{D}$, respectively. The $\tilde{A} \sim \tilde{D}$ states are the four lowest-lying singlet electronic excited-states, which are involved in building the MMVCH model. Comparisons
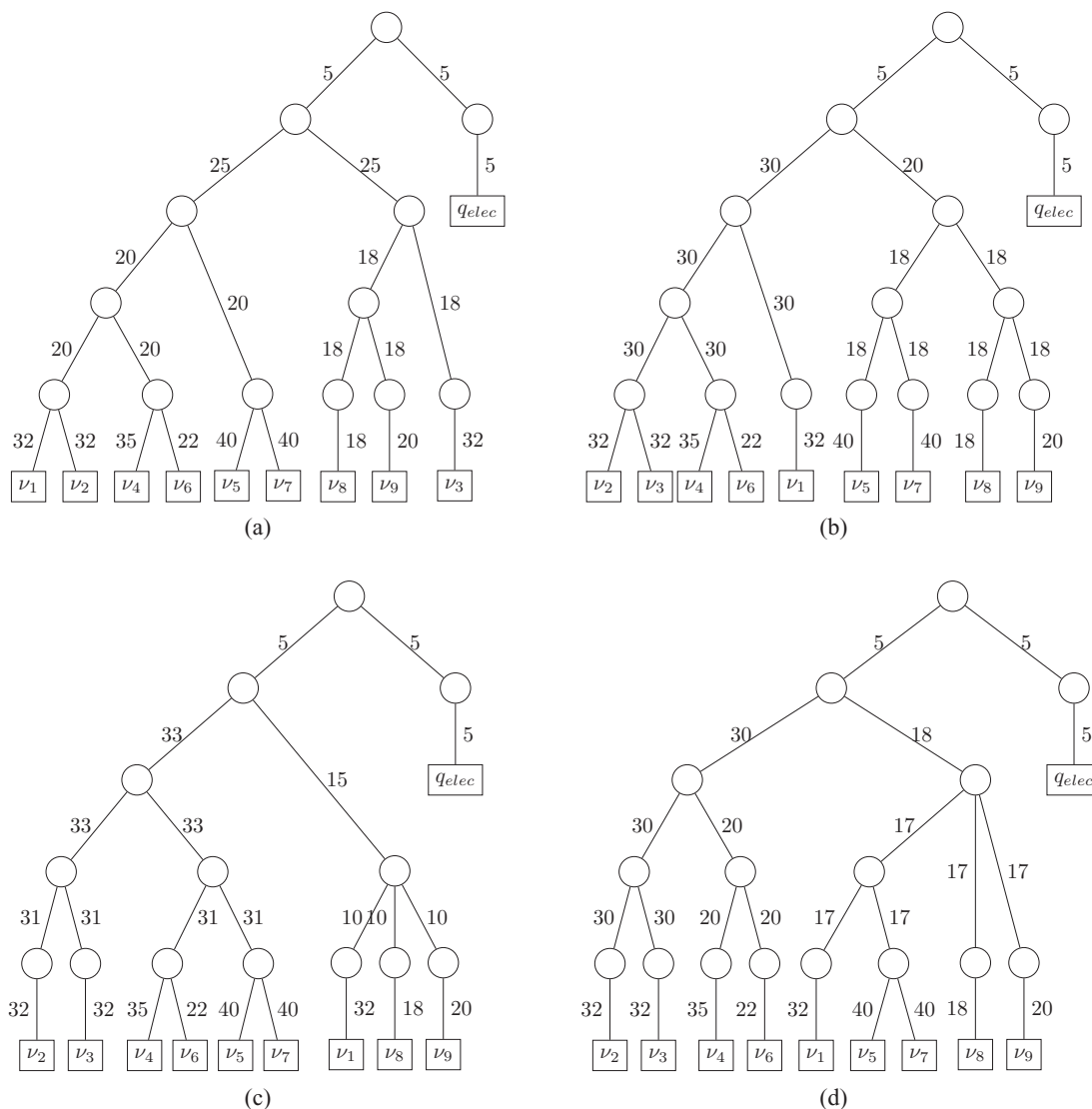
FIG. 2. The ML-MCTDH wave-function structures (ML-tree structures) for the full dimensional (9D) ML-MCTDH simulations of formaldehyde oxide, in which (a) is the ML-tree of the ML-MCTDH simulations for the $\tilde{A}\,^1A'' \leftarrow \tilde{X}\,^1A'$ band; (b) is for $\tilde{B}\,^1A' \leftarrow \tilde{X}\,^1A'$; (c) is for $\tilde{C}\,^1A' \leftarrow \tilde{X}\,^1A'$; and (d) is for $\tilde{D}\,^1A'' \leftarrow \tilde{X}\,^1A'$. The maximum depths of the trees are four layers, and the first layer separates the nine vibrational normal coordinates from the discrete electronic DOF. The number of SPFs used are shown in figures. The numbers of primitive basis functions used to represent the SPFs of the deepest layer are given next to the lines connecting with the squares.

of the present MRCI and CASSCF results with the previous TD-DFT (including TD-B3LYP, TD-BMK, and TD-M06-2X), EOM-CCSD, and CASPT2 results[6] are also given in Table I. Agreement between the present MRCI and previous EOM-CCSD[6] results is found to within typically 0.01–0.3 eV (with exception of ~0.5 eV for $\tilde{D}\,^1A''$) and taken to indicate the applicability of the MRCI energy calculations to reproduce the MMVCH model well. For TD-B3LYP, TD-BMK, and CASPT2 results,[6] however, differences between MRCI and these previous results are found to be 0.15–0.5 eV. Finally, the previous TD-M06-2X calculations[6] predicted results rather different from other calculations.

In Table II theoretical geometries of ground-state formaldehyde oxide are presented, together with the previously reported geometries.[6, 17, 18, 48, 56, 57] Experimental geometries for this molecule are not available. The present MRCI and CASSCF optimizations both predict that the ground-state formaldehyde oxide molecule is in the C_s sym-

metry with the geometry parameters (CASSCF results given in the parentheses) of $R(C - H_2) = 1.070$ Å (1.071 Å), $R(C - O_1) = 1.277$ Å (1.278 Å), $R(O_1 - O_2) = 1.355$ Å (1.349 Å), $A(H_1CH_2) = 125.2°$ (125.0°), and $A(CO_1O_2) = 117.6°$ (118.4°). Good agreement between the MRCI and CASSCF geometries is found. As shown in Table II, the present MRCI geometry parameters are also very close to the corresponding NEVPT2,[18] CCSD(T),[57] and CCSD(T)-F12a[17] results. The differences among MRCI, NEVPT2, CCSD(T), and CCSD(T)-F12a results of $R(C - O_1)$ and $R(O_1 - O_2)$ are smaller than 0.006 Å. Furthermore, good agreement among the present and previous[6, 48, 56] multiconfiguration calculations (including CASSCF and MRCI) is also found. The different basis sets used for these previous CASSCF and MRCI calculations[6, 48, 56] should be the source the slight differences of <0.03 Å for $R(C - O_1)$ and $R(O_1 - O_2)$. Finally, the B3LYP calculation[48] gives a rather small value for $R(C - O_1)$ and larger value for $A(CO_1O_2)$.

TABLE I. MRCI and CASSCF results for the vertical excitation energies (E_v, in eV) of electronic states (including singlet and triplet states below 8.0 eV) of formaldehyde oxide based on the corresponding MRCI and CASSCF optimized geometries of ground States (see Table II). Note that no experimental geometry for formaldehyde oxide is available in the literature. The second, third, and fourth columns give the E_v values of each state based on MRCI(14e,12o), MRCI(8e,8o), and previous MRCI(12e,11o) calculations, respectively. The fifth, sixth, and seventh columns give the E_v values using the CASSCF(14e,12o), CASSCF(8e,8o), and previous CASSCF(12e,11o) calculations. The other columns contain the previously reported TD-DFT, EOM-CCSD, and CASPT2 E_v values. The right-most column gives the character of the states according to the character of the configurations based on the present MRCI calculation.

	E_v/eV		
	\multicolumn{3}{c}{MRCI}		\multicolumn{3}{c}{CASSCF}			\multicolumn{3}{c}{TD-DFT[b]}	CASPT2			
States	(14e,12o)[a]	(8e,8o)[a]	(12e,11o)[b]	(14e,12o)[a]	(8e,8o)[a]	(12e,11o)[b]	B3LYP	BMK	M06-2X	(12e,11o)[b]	EOM-CCSD[b]	Expt.	Character[c]
$\tilde{X}\,^1A'$	0.00	0.00	0.00	0.00	0.00	0.00	0.00	0.00	0.00	0.00	0.00	0.00	PS
$\tilde{a}\,^3A'$	1.81	1.87		1.98	1.83								SUS
$\tilde{b}\,^3A''$	2.48	2.65		2.56	2.68								SUS
$\tilde{A}\,^1A''$	2.57	2.70		2.63	2.73		2.50	2.87	2.28	2.22	2.80		TMCS
$\tilde{B}\,^1A'$	4.03	3.89	3.93	4.26	4.42	4.16	4.32	4.55	2.95	3.18	4.04	3.70[d], 3.49[e], 3.65[f]	TMCS
$\tilde{C}\,^1A'$	6.96	6.82			7.14		6.08	6.57	3.78	6.34	6.52		TMCS
$\tilde{D}\,^1A''$	7.01	7.08		7.60	8.09		6.08	6.68	3.76	6.37	6.50		TMCS

[a]Present work.

[b]Reference 6.

[c]An electronic state is characterized[60] as a primary state (PS) or shake-up state (SUS) if its wave function has a dominant primary-configuration or a dominant shake-up configuration with the weight larger than 0.85. If an electronic state has no dominant configuration in its wave function, it is characterized as a typical multiconfigurational state (TMCS). At the HF/STO-3G level, the ground-state formaldehyde oxide has the electronic configuration $\cdots(6a')^2(7a')^2(8a')^2(1a'')^2(9a')^2(10a')^2(2a'')^2(3a'')^0(11a')^0(12a')^0(13a')^0(14a')^0$.

[d]Evaluated from the experimental UV spectrum of formaldehyde oxide isolated in a pulsed supersonic expansion (see Ref. 5).

[e]Evaluated from the UV absorption spectrum of formaldehyde oxide (see Ref. 10).

[f]Evaluated from the UV absorption spectrum measured in a jet-cooled molecular beam (see Ref. 16).

2. Parameters of the MMVCH model

To determine the ground-state vibrational frequencies ω_i and the ith normal mode coordinate q_i in the MMVCH model, the CASSCF vibrational frequency calculations are carried out by using the CASSCF and MRCI geometries. Since the CASSCF and MRCI geometries are close to each other, no imaginary frequency is predicted by using both CASSCF and MRCI geometries. These CASSCF frequencies calculations

give nine normal vibrational modes ($7a' \oplus 2a''$), which are the coordinates q_i of the MMVCH model. These results, including ω_i and their symmetry plus the simple description of q_i, together with theoretical[17,18,56,57] and IR experimental[18] frequencies are collected in Table III. In the present work, the CASSCF//MRCI vibrational frequencies ω_i and the corresponding normal modes q_i are used to build the MMVCH model.

TABLE II. MRCI and CASSCF optimized geometries for formaldehyde oxide in the ground state. Here bond lengths are given in angstrom, whereas, the angle values are given in degree (for notations see Figure 1). Previously reported theoretical geometries are also given. Note that no experimental geometry for formaldehyde oxide is available in the literature.

	Geometry	
Methods	$R(C-H_2)$	$R(C-O_1)$	$R(O_1-O_2)$	$A(H_1CH_2)$	$A(CO_1O_2)$	Reference
MRCI/aVTZ[a]	1.070	1.277	1.355	125.2	117.6	Present work
CASSCF/aVTZ[a]	1.071	1.278	1.349	125.0	118.4	Present work
CASSCF/VTZ[a]	1.094	1.270	1.361	124.7	117.7	Present work
NEVPT2/aVTZ		1.277	1.349			18
CCSD(T)/aVTZ		1.275	1.349			57
CCSD(T)-F12a/aVTZ	1.079	1.270	1.342	126.5	117.8	17
MRCI/VDZ[b]	1.085	1.280	1.322	126.0	119.0	56
CASSCF/VDZ[b]	1.104	1.281	1.356	125.1	117.9	56
CASSCF/6-311+G(2d,2p)[c]		1.276	1.363		117.3	48
CASSCF/unAVDZ[d]		1.278	1.347		117.0	6
CASSCF/aVTZ[d]		1.279	1.346		118.3	6
B3LYP/6-311+G(2d,2p)		1.254	1.352		119.2	48

[a]The (8e,8o) active space is used in the CASSCF and MRCI calculations.

[b]The active spaces of (14e,12o) and (8e,6o) were used in the CASSCF and MRCI (denoted as "CAS+1+2" there) calculations, respectively (see Ref. 56 for details).

[c]The (10e,10o) active space was used in the CASSCF calculations (see Ref. 48 for details).

[d]The (12e,11o) active space was used in the CASSCF calculations. The abbreviations of "unAVDZ" and "unAVTZ" stand for the uncontracted aug-cc-pVDZ and aug-cc-pVTZ basis sets, respectively (see Ref. 6 for details).

TABLE III. Vibrational frequencies (in cm^{-1}) of formaldehyde oxide in ground state performed in the present work (given in the third, fourth, fifth, and sixth columns) and in the previous studies, together with symmetry (given in the second column) and description (given in the right most column) of each vibrational mode. Since the formaldehyde oxide molecule is at the C_s symmetry, the vibrational reducible representation can be reduced to $7a' \oplus 2a''$. The second last column gives the experimental results. Here, theoretical frequencies are harmonic, whereas, experimental ones are fundamental, unless otherwise specified.

Modes[a]	Symm.	Vibrational frequencies (in cm^{-1})								Description
		MRCI[b]	CAS[b]	CAS[c]	CCSD(T)[d]	NEVPT2[e]	CCSD(T)-F12a[f]	VCI-5[g]	Expt.[h]	
ν_1	a'	563.92	546.27 (533.37)	537	529	536 (530)	536 (536)	526		COO deform
ν_2	a''	645.94	570.78 (636.71)	618	632	620 (606)	639 (642)	622		CH$_2$ twist
ν_3	a''	832.89	907.33 (864.94)	793	862	856 (853)	878 (872)	859	848	CH$_2$ wag
ν_4	a'	899.08	918.56 (842.19)	849	935	916 (892)	951 (949)	927	908	OO stretch
ν_5	a'	1252.90	1246.86 (1245.59)	1233	1231	1235 (1220)	1240 (1241)	1212	1241	CH$_2$ rock
ν_6	a'	1331.66	1292.25 (1300.40)	1269	1306	1338 (1302)	1317 (1321)	1285	1286	CO stretch/CH$_2$ scissor
ν_7	a'	1586.99	1531.36 (1493.11)	1465	1483	1500 (1458)	1490 (1488)	1434	1435	CH$_2$ scissor/CO stretch
ν_8	a'	3303.31	3181.21 (3039.12)	3065	3137	3197 (3030)	3141 (3137)	3013		CH symmetric stretch
ν_9	a'	3461.19	3326.61 (3179.09)	3215	3290	3370 (3149)	3302 (3300)	3151		CH asymmetric stretch

[a]The order of vibrational modes are determined by the present CASSCF/aVTZ calculation.
[b]Present work. "MRCI" stands for the "CASSCF/aVTZ//MRCI/aVTZ" calculations. "CASSCF/aVTZ" is abbreviated as "CAS". The CASSCF/VTZ results are given in the parentheses.
[c]"CAS" means "CASSCF(14e,12o)" and the VDZ basis set was used (see Ref. 56 and references therein for details).
[d]The aTVZ basis set was used in the CCSD(T) calculations (see Ref. 57 and references therein for details).
[e]The aVDZ basis set was used. Given in parentheses are the anharmonic wave numbers at the NEVPT2/aVDZ level (see Ref. 18 for details).
[f]The aVTZ basis set was used. Given in parentheses are the frequencies evaluated from the ground-state PES fitted by permutation invariant polynomial neural network (PIP-NN) method (see Ref. 17).
[g]The frequencies were calculated by using the vibrational configuration interaction (VCI) with up to 5-mode excitations on the basis of the PIP-NN PES (see Ref. 17 for details).
[h]Evaluated from the infrared absorption spectrum (see Ref. 18 for details).

Although the MRCI and NEVPT2 geometries are close to each other (see Table II), agreement between the CASSCF//MRCI and NEVPT2[18] frequencies is found to within 30 cm^{-1} and $\sim$100 cm^{-1} for low ($\nu_1 - \nu_6$) and high ($\nu_7 - \nu_9$) frequency modes, respectively. Such higher differences ($\sim$100 cm^{-1}) for the ν_7, ν_8, and ν_9 modes may occur because (i) the MRCI geometry is not the real minimum of the CASSCF PES and (ii) the basis set (aVTZ) used in the CASSCF//MRCI is larger than aVDZ used in the NEVPT2 calculations.[18] For example, the differences for all modes between the CASSCF and corresponding NEVPT2[18] frequencies are smaller than 60 and 50 cm^{-1} using aVTZ and aVDZ, respectively. In addition, for ν_3, ν_4, and ν_5 the deviations between the CASSCF//MRCI and IR experimental[18] are smaller than 15 cm^{-1}. However, for ν_6 and ν_7 such deviations are 50 and <150 cm^{-1}, respectively, which may occur because the ν_6 and ν_7 modes are anharmonic. For example, the anharmonic NEVPT2 frequencies[18] for ν_6 and ν_7 are close to the corresponding IR values[18] while the harmonic results[18] are $\sim$70 cm^{-1} larger than IR values.[18] Similarly, the present CASSCF//MRCI frequencies are close to the corresponding CCSD(T)-F12a[17] results for $\nu_1 - \nu_6$, while the CASSCF//MRCI frequencies for $\nu_7 - \nu_9$ are $\sim$100 or $\sim$160 cm^{-1} larger the corresponding CCSD(T)-F12a[17] results. Similar differences can also be found when comparing the present CASSCF//MRCI and previous CCSD(T)[57] results.

The various coupling constants are calculated by using finite displacements along the various normal coordinates q_i. While for the totally symmetric modes first- and second-order derivatives are needed for the intra-state coupling constants, the computation of the inter-state coupling constants requires the second derivatives along an appropriate normal coordinate. These are defined in relation to the

MMVCH model and are obtained by MRCI calculations without further readjustment. The MRCI calculations reveal that not all vibrational modes of the systems play a significant role in the vibronic coupling mechanism because of small coupling constants. This holds, e.g., for both CH symmetric and asymmetric stretching modes (ν_8 and ν_9, respectively). The vibrational modes with most significant coupling constants are considered to play a more important role and thus are set to have larger DVR and SPF sizes for easier convergence of the dynamics calculations. As already noted, all normal vibrational modes (nine nuclear DOFs) are considered in the present work. All couplings constants are given in Table IV.

B. MCTDH and ML-MCTDH dynamics simulations

Having derived the parameters on the MMVCH model, we shall discuss the MCTDH and ML-MCTDH simulation results on the UV spectrum of formaldehyde oxide. Before showing the spectral results, let us first show the numerical results of the MCTDH and ML-MCTDH simulations and discuss the computational efficiency of MCTDH and ML-MCTDH for this 9D system.

1. Numerical results

Based on the optimized ML-trees (as shown in Figure 2), the ML-MCTDH calculations are performed in full dimensionality. Additionally, to compare the MCTDH efficiency with ML-MCTDH, we also perform the full dimensional MCTDH calculations using the multi-set formalism and the mode-combination schemes of (ν_2, ν_3), (ν_6, ν_8), (ν_4, ν_5, ν_7), and (ν_1, ν_9). The parameters and numerical results, including

TABLE IV. Intra-state linear $\kappa_j^{(I)}$ and quadratic $\gamma_j^{(I)}$ coupling constants ($j \in A'$) entering the MMVCH model for formaldehyde oxide (the upper panel), together with the linear inter-state coupling parameters $\lambda_j^{(J,K)}$ (the lower panel) where $\Gamma_J \otimes \Gamma_j \otimes \Gamma_K \supset A'$. For each mode of one electronic excited-state, the quadratic coupling constants are given in italic. The order for the vibrational modes is given according to the CASSCF/aVTZ calculation. All coupling quantities are in 10^{-4} a.u.

	Intra-state linear and quadratic coupling parameters			
Modes	$\tilde{A}\ ^1A''$	$\tilde{B}\ ^1A'$	$\tilde{D}\ ^1A''$	$\tilde{C}\ ^1A'$
ν_1	3.12, *0.56*	14.89, *0.41*	2.95, *0.37*	1.87, *0.35*
ν_4	−4.37, *3.75*	−41.09, *5.20*	−51.88, *2.79*	−116.53, *−5.42*
ν_5	16.18, *7.04*	−9.11, *7.47*	4.66, *5.68*	−36.37, *4.00*
ν_6	24.32, *5.83*	24.82, *5.83*	26.51, *4.07*	10.26, *4.36*
ν_7	−8.53, *8.26*	−4.40, *7.98*	−16.93, *7.10*	4.58, *5.43*
ν_8	0.21, *36.44*	−8.19, *36.73*	−2.60, *36.26*	−15.26, *33.83*
ν_9	0.44, *39.88*	2.66, *40.41*	1.75, *39.56*	−18.79, *31.80*

	Inter-state linear coupling parameters									
Modes	$\tilde{X}\sim\tilde{A}$	$\tilde{X}\sim\tilde{B}$	$\tilde{X}\sim\tilde{D}$	$\tilde{X}\sim\tilde{C}$	$\tilde{A}\sim\tilde{B}$	$\tilde{A}\sim\tilde{D}$	$\tilde{A}\sim\tilde{C}$	$\tilde{B}\sim\tilde{D}$	$\tilde{B}\sim\tilde{C}$	$\tilde{C}\sim\tilde{D}$
ν_1		27.01		40.94		15.64			30.76	
ν_2	40.64		82.99		16.26		24.68	90.97		89.05
ν_3	64.87		60.77		55.57		69.66	69.37		112.93
ν_4		57.75		99.74		34.68			115.25	
ν_5		54.18		37.49		41.20			65.89	
ν_6		21.71		36.97		46.90			42.88	
ν_7		15.93		54.17		37.93			56.46	
ν_8		24.25		55.05		14.96			60.16	
ν_9		15.12		102.60		20.29			103.71	

SPF sizes, CPU time, and total number of coefficients of the various calculations are given in Table V.

Because the vibrational normal modes are used as coordinates in the present work, in all dynamics simulations the harmonic oscillator (Hermite) functions are used as the primitive basis functions which meet the physical meanings of the coordinates. The size of the primitive basis for each modes are given in Figure 2 next to the lines connecting with the squares and are also collected here as 32, 32, 32, 35, 40, 22, 40, 18, and 20 for ν_1 to ν_9, respectively. The identical size of the primitive basis set is used in both MCTDH and ML-MCTDH simulations. More difficult is to determine a well adapted ML-tree for the ML-MCTDH calculations. An iterative scheme[53] is adopted to optimize the ML-tree. For two lowest-lying singlet states $\tilde{X}$ and $\tilde{A}$, the identical ML-tree parameters, including the structure of ML-tree and the SPF sizes of each mode, are used similar as done in studies on difluorobenzene,[53] naphthalene, and anthracene cations.[54] For other states, different parameters are determined iteratively.[53,54] The SPF sizes for MCTDH calculations, collected in Table V, are also carefully checked to ensure convergence.

As shown in Table V, the CPU times of the ML-MCTDH calculations for all electronic states (in the range of 2–7 h) are much lower than the corresponding CPU times of the MCTDH calculations (19–24 h). Due to the fact that the number of total coefficients used to expand the wave-function is much less for ML-MCTDH calculations (10^4–10^5) as compared to MCTDH calculations ($\sim 10^6$), the total memory need for ML-MCTDH (less than 55 megabyte) is much smaller than that for MCTDH (~ 750 megabyte). Furthermore, as

shown in the supplementary material,[58] both ML-MCTDH and MCTDH simulations provide identical spectra. The numerical results indicate that for the present 9D MMVCH model, the ML-MCTDH calculations save a considerable amount of computational resources.

For a system with a dimensionality of 18 or more, a higher efficiency of ML-MCTDH is expected.[28] By the present comparison between our MCTDH and ML-MCTDH numerical results, it is shown that the ML-MCTDH method is still more efficient than MCTDH in case of the present 9D MMVCH model. One can hence expect that systems with nine or more DOFs can be simulated preferably by ML-MCTDH. However, we would like to emphasize that the computational efficiency actually depend on the system itself (for example, the couplings among the degrees of freedom, the PES, grid sizes, and so on), but not on the dimensionality alone. However, the dimensionality is indeed an important criterion for easily indicating the system size and computational complexity.

2. Spectral features

As given in Sec. II, the spectra of each electronic states are calculated through Fourier transformation of the auto-correlation functions $C(t) = \langle \Psi(0)|\Psi(t)\rangle$ which are obtained by propagating the nuclear wave functions using full dimensional ML-MCTDH and MCTDH simulations. In both cases, the Hamiltonian is based on the MMVCH model computed at the MRCI level. Shown in Figure 3 are the

TABLE V. Simulation parameters of the 9D ML-MCTDH and MCTDH calculations for each electronic excited states of formaldehyde oxide using the MMVCH model. The third column contains the CPU time (in the format of hour:minute) of each ML-MCTDH and MCTDH simulations using a total propagation time of 200 fs. All simulations were run on the same machine and CPU type (Intel® Xeon® CPU E5520, 2261 MHz) using a single core. The fourth column shows the total number of time-dependent coefficients propagated in each case. The fifth column contains, for ML-MCTDH simulations, the number of SPFs for each node of the tree according to the representation in ML-tree figures (see Figure 2). The parentheses in the square brackets indicate that different SPF numbers are taken for each of the branches. For the MCTDH calculations, we use different sets of SPFs for each electronic state, namely the multi-set formalism. Thus, for MCTDH calculations of each electronic state, the fourth column contains in square brackets the numbers of SPFs for combined modes: (ν_2, ν_3), (ν_6, ν_8), (ν_4, ν_5, ν_7), and (ν_1, ν_9), respectively. The right most column shows the total memory (in megabyte, mb) used during the calculations.

State	Method	CPU time	Total coefficients	Numbers of SPFs	Memory
$\tilde{X}\,^1A'$	ML-MCTDH	2:11	35082	[25;20,18;20,18]	30
	MCTDH	21:49	1214120	[4,3,4,3]	745
$\tilde{A}\,^1A''$	ML-MCTDH	2:07	35082	[25;20,18;20,18]	30
	MCTDH	23:59	1214120	[4,3,4,3]	745
$\tilde{B}\,^1A'$	ML-MCTDH	5:31	74221	[(30,20);30,18;30,18,18]	36
	MCTDH	24:22	1214120	[4,4,4,3]	745
$\tilde{C}\,^1A'$	ML-MCTDH	6:36	116863	[(33,15);33,10;31,31]	53
	MCTDH	20:23	1214120	[4,4,4,3]	745
$\tilde{D}\,^1A''$	ML-MCTDH	3:25	70753	[(30,18);(30,20),17;30,20,17,17]	30
	MCTDH	18:57	1214120	[4,4,5,3]	745

simulated UV spectra bands for various transitions. The relevant energy ranges cover all of the electronic states, spectral features above ∼8.0 eV are irrelevant for our purpose.

On the basis of the CASSCF calculations, the oscillator strengths for the $\tilde{A} \leftarrow \tilde{X}$, $\tilde{C} \leftarrow \tilde{X}$, and $\tilde{D} \leftarrow \tilde{X}$ transitions are all equal to zero (as also suggested by Lee *et al.*[6]), which implies that the $\tilde{A}\,^1A''$, $\tilde{C}\,^1A'$, and $\tilde{D}\,^1A''$ states are dark states. The intensities of these three bands in the UV spectrum must be very small. Since only the $\tilde{B} \leftarrow \tilde{X}$ transition (oscillator strength is ∼800 cm^{-1}) is observed,[5,10,16] we shall discuss only this band in detail in Sec. III C.

When computing the summed UV excitation spectra, the individual oscillator strengths must be included. For dark state, its weight in the summed spectrum is very small and its spectral intensity is near zero. Since the spectral bands for the $\tilde{A} \leftarrow \tilde{X}$, $\tilde{C} \leftarrow \tilde{X}$, and $\tilde{D} \leftarrow \tilde{X}$ transitions are dark, a summed spectrum are not drawn here. Just individual $\tilde{A}$, $\tilde{C}$, and $\tilde{D}$ spectra are then given in Figure 3. In principle, the spectra of the dark states can be measured by exciting formaldehyde oxide through, e.g., electron collisions.

As already noted, identical spectra are produced by both the ML-MCTDH and MCTDH calculations (see supplementary material[58]). For clarity, therefore, the MCTDH spectra are not given. Because of the large vibronic couplings and similar vertical excitation energies of the $\tilde{C}$ and $\tilde{D}$ states (6.82 and 7.08 eV, respectively), the spectrum has a much broader $\tilde{C} \sim \tilde{D}$ band with more complex vibronic structures than the other spectra bands. Therefore, two individual spectra of the $\tilde{A}$ and $\tilde{C} \sim \tilde{D}$ bands are shown in Figure 3. For $\tilde{C}\,^1A'$ and $\tilde{D}\,^1A''$ the nonadiabatic coupling causes a strong mixing of their vibrational energy levels so that the vibronic bands become more overlapping and complex, while the situation of the $\tilde{A}$ and $\tilde{B}$ bands are different. These bands are well separated, which suggests that the vibronic couplings among $\tilde{X}$, $\tilde{A}$, and $\tilde{B}$ is comparatively small. It is however interesting to

note that one must not ignore the $\tilde{C}$ and $\tilde{D}$ states when computing the $\tilde{A} \leftarrow \tilde{X}$ or $\tilde{B} \leftarrow \tilde{X}$ spectra, the high lying states have a non-negligible effect.

From the simulated spectrum, on the other hand, the excitation energies of $\tilde{A}\,^1A''$, $\tilde{C}\,^1A'$, and $\tilde{D}\,^1A''$ are given as 2.74, 6.74, and 7.15 eV, respectively. These spectral excitation energies are very close to the corresponding MRCI excitation energies of 2.70, 6.82, and 7.08 eV. In addition, the theoretical spectral band for $\tilde{B} \leftarrow \tilde{X}$ (see Sec. III C below) predicts the excitation energy of 3.71 eV which is very close to the experimental values of 3.49 ∼ 3.70 eV[5,10,16] (see also Table I).

C. Discussions on the $\tilde{B}\,^1A' \leftarrow \tilde{X}\,^1A'$ spectral band

Since the $\tilde{B}\,^1A'$ state is the only bright state, the $\tilde{B} \leftarrow \tilde{X}$ band plays an important role for detecting the formaldehyde oxide molecule in a reaction pool. Recently, three laboratory recordings for this band[5,10,16] became available. The present full dimensional ML-MCTDH band is presented in Figure 4 along with these three experimental spectra.[5,10,16] After exploring the deviations among the theoretical and three experimental[5,10,16] spectra, we shall discuss possible reasons for these deviations.

1. Deviations between the ML-MCTDH and experimental spectral bands

As shown in Figure 4, the black, bright blue, purple, blue, and green lines represent the present ML-MCTDH spectrum, the spectrum reported by Beames *et al.*,[5] the Gaussian fitted spectrum of Beames *et al.*,[5] Sheps' spectrum[10], and the spectrum of Ting *et al.*[16] For easily comparing, the intensities of these experimental spectra are scaled to that of the ML-MCTDH band.
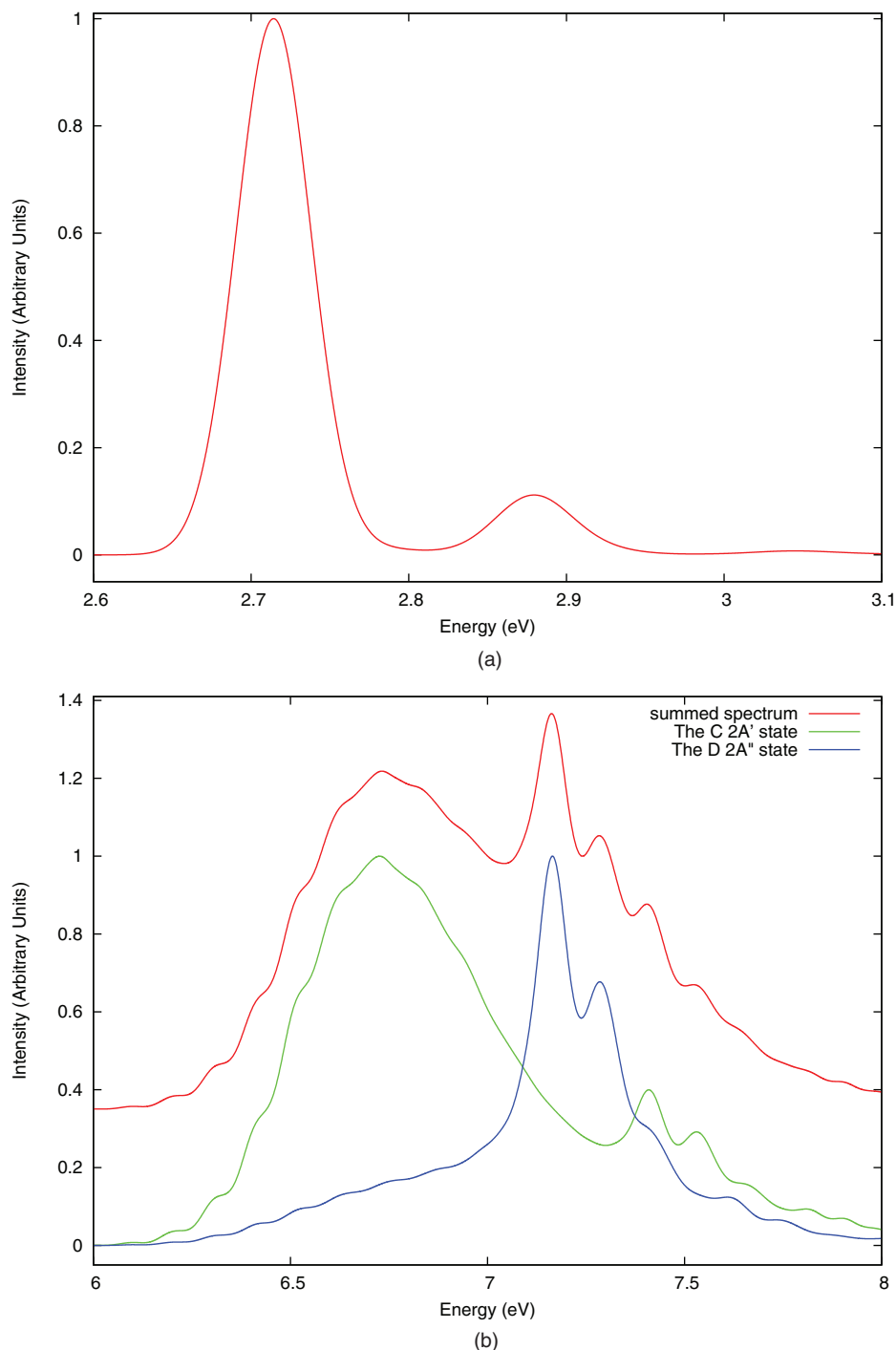
FIG. 3. The ML-MCTDH band-spectra for the (a) $\tilde{A}\,^1A'' \leftarrow \tilde{X}\,^1A'$, (b) $\tilde{C}\,^1A' \leftarrow \tilde{X}\,^1A'$, and $\tilde{D}\,^1A'' \leftarrow \tilde{X}\,^1A'$ transitions based on the full dimensional (9D) dynamics simulations. These ML-MCTDH spectra are obtained by a Fourier-transform of the auto-correlation function and are broadened by convoluting them with a Gaussian function. The resulting resolution is 55 meV FWHM (full width at half maximum). In the lower part of panel (b) the green and blue lines represents the 9D ML-MCTDH spectra of $\tilde{C}\,^1A'$ and $\tilde{D}\,^1A''$ bands, while the summed spectrum for the $\tilde{C} \sim \tilde{D}$ band is given in the upper part of panel (b). The MCTDH and ML-MCTDH simulations provide identical spectra. For clarity, the 9D MCTDH spectra are not shown here.

In 2012, UV excitation for $\tilde{B} \leftarrow \tilde{X}$ was measured by Beames *et al.*[5] as a ground-state population depletion of formaldehyde oxide, which is detected by single-photon ionization at 118 nm (10.5 eV). In this experiment,[5] formaldehyde oxide was synthesized through

$$CH_2I_2 \xrightarrow{248\,nm} CH_2I + I$$
$$CH_2I + O_2 \rightarrow CH_2OO + I \tag{4}$$
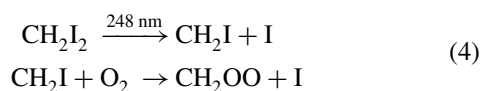
in a flow cell at low pressures. The whole process of their experiment[5] can be written as $\cdots \rightarrow CH_2OO\,(\tilde{X}\,^1A')$ $\xrightarrow{335\,nm} CH_2OO\,(\tilde{B}\,^1A') \xrightarrow{118\,nm} CH_2OO^+$. In fact what is observed in the experiment of Beames *et al.*[5] is an action spectrum of $\tilde{B} \leftarrow \tilde{X}$ band.

In addition, two absorption spectra for $\tilde{B}$ band were measured. In 2013, the transient absorption in the range of 2.76–4.13 eV (300–450 nm) was measured by Sheps[10] in a
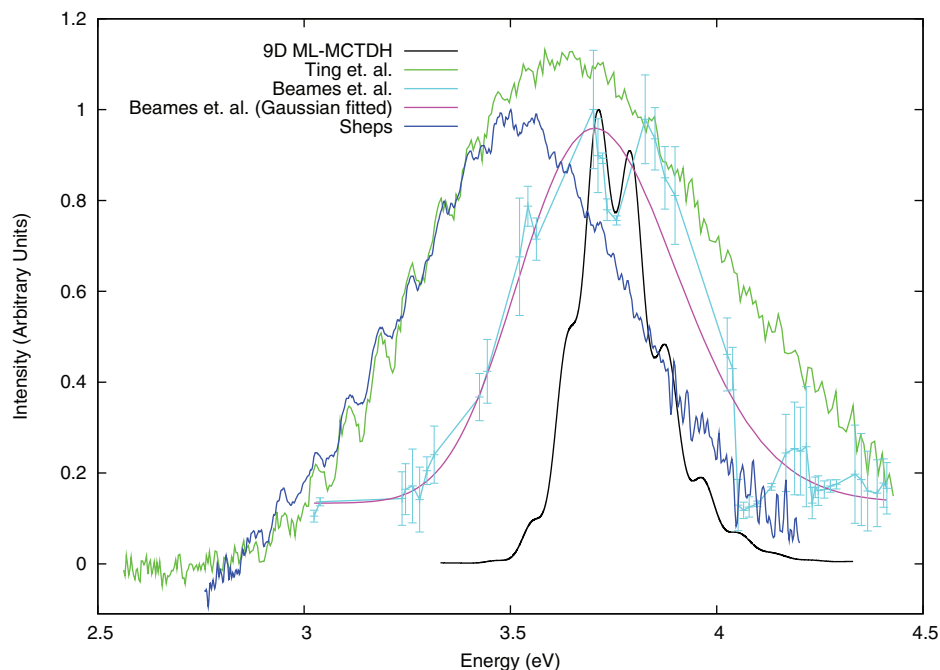
FIG. 4. Comparison of the 9D ML-MCTDH theoretical vs the experimental UV absorption spectra[5,10,16] of the $\tilde{B}\,^1A'$ band of formaldehyde oxide. The 9D ML-MCTDH theoretical spectrum is obtained via a Fourier-transform of the auto-correlation function. The spectrum is then broadened by convoluting it with a Gaussian. The resulting resolution is 55 meV FWHM. The experimental UV spectrum and its Gaussian fit drawing in the bright blue and purple lines, respectively, are reprinted with permission from Beames *et al.*, J. Am. Chem. Soc. **134**, 20045 (2012). Copyright 2012 American Chemical Society. The experimental UV spectrum drawn in the blue line is reprinted with permission from L. Sheps, J. Phys. Chem. Lett. **4**, 4201–4205 (2013). Copyright 2013 American Chemical Society. The experimental UV spectrum drawing in the green line is reprinted with permission from Ting *et al.*, Phys. Chem. Chem. Phys. **16**, 10438 (2014). Copyright 2014 The Owner Societies.

time-resolved cavity-enhanced absorption spectrometer, using a gas-phase reactor coupled to a broadband optical resonator. Here formaldehyde oxide was synthesized by reaction (4) but using the photon of 266 nm[10] to prepare CH_2I. In 2014, Ting *et al.*[16] prepared formaldehyde oxide in a pulse-photolysis cell following reaction (4) at 248 nm. The transient absorption for $\tilde{B} \leftarrow \tilde{X}$ were then recorded by a gated intensified charge-coupled device (CCD) camera when the probe light have been dispersed by a grating monochromator.[16] Since the same UV absorption process was involved in these two experiments[10,16] agreement exists between two absorption spectra at the low-energy side, while the faster decay of Sheps' spectrum[10] at the high-energy side may arise from the different methods used in the two experiments.[10,16]

As shown in Figure 4, or in Figure 4 of Ref. 16, the absorption spectra of Sheps[10] and Ting *et al.*[16] show very similar fine structure features in the lower-energy side (<3.49 eV), while both of these spectra have a large number of fine structures in the higher-energy side (>3.5 eV) but with very different intensities. The excitation energy of 3.49 eV suggested by Sheps[10] is then 0.16 eV smaller than that suggested by Ting *et al.*[16] (3.65 eV). The present ML-MCTDH absorption spectrum band has a much smaller spectral-width at half maximum. As shown in Figure 4, in the higher-energy side (>3.71 eV) the ML-MCTDH band is characterized by a rather resolved and regular structure with one remarkable peak at 3.79 eV plus three small peaks at ~3.87, ~3.97, and ~4.05 eV, whereas the lower-energy side (<3.71 eV) exhibits a diffuse spectral envelope. This indicates that there is no conical intersection between $\tilde{B}$ and other states near

the Franck-Condon region. Indeed, the MRCI calculations for the MMVCH model along the normal mode directions show no crossing-point among the potential energy curves. On the other hand, the action spectrum of Beames *et al.*[5] also predicts two remarkable peaks at 3.70 and 3.83 eV (main peak and the second peak, respectively), which are close to the present theoretical peaks of 3.71 and 3.79~3.87 eV. Furthermore, the experimental spectrum of Beames *et al.*[5] show somewhat closer lying peaks at ~3.3, ~3.4, ~3.6, 3.7~3.9, and ~4.0 eV. These peaks may correspond to the tiny peaks (or plateaus) in the ML-MCTDH spectrum at ~3.6, ~3.87, and ~3.97 eV.

In summary, both the absorption spectra[10,16] show very similar fine structures in the lower-energy side (<3.49 eV) but give very different intensities in the higher-energy side (>3.5 eV). Moreover, the spectrum of Beames *et al.*,[5] an action spectrum, approaches the absorption spectra of Ting *et al.*[16] in the higher-energy side (>3.71 eV) but fast decays in the lower-energy side (<3.4 eV).

2. Possible reasons for the deviations

As discussed above, the UV action[5] and absorption[10,16] spectra exhibit significant differences. It is surprising that, however, the present ML-MCTDH absorption spectrum is similar to the action spectrum[5] but with a rather small spectral-width at half maximum.

The reasons for the deviations may be manifold. First, as discussed by Ting *et al.*[16] the temperature effect may be one possible reason. In all experiments, the temperature of the photolysis-synthesis cell was ~295 K, while formaldehyde

oxide beam in the experiment of Beames *et al.*[5] was jet-cooled to ∼10 K. If temperature can strongly affect the spectral intensity in the range of <3.44 eV (>360 nm) as it does in the case of the Huggins or the Hartley band of ozone (smaller intensity at lower temperature),[59] then it can explain the weaker spectrum of Beames *et al.*[5] in this this region. Turning to the ML-MCTDH spectrum we note that the *ab initio* quantum dynamics simulations are performed assuming zero temperature. Therefore, the lack of quantum-statistical temperature effects may cause the too small spectral-width exhibited in Figure 4. However, it does not seem likely that temperature effects are strong enough to broaden the spectrum by ∼0.4 eV.

Second, the photolysis of the $\tilde{B}\,^1A'$ state may strongly influence the experimental results. As discussed by Sheps[10] the lower-intensity of the action spectrum[5] in the lower-energy side is caused by a decrease in the dissociation yield of $\tilde{B}\,^1A'$. However, using velocity map ion imaging, Lehman *et al.*[9] reported that the UV photodissocoation of formaldehyde oxide in $\tilde{B}\,^1A'$ is faster than its rotation, which is inconsistent with the discussions of Sheps.[10] Thus, another faster process than photodissocoation is required if Sheps' discussion[10] can work. An extremely rapid self-reaction of formaldehyde oxide[15] was recently reported, which implies that such a fast process may occur. However, more experimental and theoretical investigations are still needed.

Third, from the computation-technical point of view, the small spectral-width value at half maximum may be caused by missing some couplings in the model Hamiltonian. As shown in Sec. II, however, all nine normal modes and all possible inter- and intra-state vibronic couplings are included in the present MMVCH model based on the high-level MRCI calculations. Therefore, although the model parameters are expected to be correct, the model itself may be insufficient and the inclusion of higher order couplings may be necessary. In the present moment, we believe that such higher-order vibronic couplings are unimportant because they are generally weak. Other kinds of coupling, for example, the spin-orbit coupling between singlet and triplet states, is also expected too weak as to cause a significant broadening of the spectrum.

Finally, the deviations among the experimental spectra, where the spectra of Sheps[10] and Ting *et al.*[16] match each other in the lower-energy side and the spectra of Beames *et al.*[5] and Ting *et al.*[16] match each other in the higher-energy side, implies the complexity to synthesize, to handle, and to measure spectrum for this recently prepared molecule. There are many potential impurities in the synthesis and/or reaction cell, including CH_2I_2, CH_2I, SO_2, O_2, and so on. Although they cannot change the spectrum of formaldehyde oxide at the experimental conditions, they would react with formaldehyde oxide or quench it before the system approaching the light pulse. In addition, the extremely rapid self-reaction of formaldehyde oxide,[15] as discussed above, may also quench itself and influence the spectrum.

IV. CONCLUSIONS

In the present work, the full dimensional MCTDH and ML-MCTDH vibronic dynamics of the simplest Criegee intermediate, formaldehyde oxide, in the five lowest-lying singlet electronic states are reported based on the MMVCH model. The MMVCH model is based on extensive MRCI(8e,8o)/aug-cc-pVTZ energy calculations. When the MMVCH model is built, a large number of ML-MCTDH test calculations are performed to find appropriate ML-trees, and the convergence is carefully checked to ensure accurate results. To compare the computational efficiencies between the MCTDH and ML-MCTDH methods for the present 9D system, MCTDH simulations using the same Hamiltonian are also performed. The numerical results of the MCTDH and ML-MCTDH calculations imply that even for the present not-too-large 9D system the ML-MCTDH calculations can also save a considerable amount of computational resources and produce identical spectra as the MCTDH calculations. Furthermore, on the basis of the present full dimensional ML-MCTDH and MCTDH calculations, the UV absorption spectra are simulated. To the best of our knowledge, this is the first theoretical UV spectrum simulated for this molecule including nuclear motion beyond an (adiabatic) harmonic approximation. The $\tilde{B}\,^1A' \leftarrow \tilde{X}\,^1A'$ band from the present 9D ML-MCTDH calculation is also compared with experimental measurements.[5,10,16] Qualitative agreement between the present theoretical $\tilde{B} \leftarrow \tilde{X}$ band and the experimental measured bands[5,10,16] is found.

The full dimensional ML-MCTDH calculations consume much less computational resources (including smaller memory space and shorter single CPU-time) than corresponding MCTDH calculations, but they yield identical spectra. These facts indicate the preferable efficiency of the ML-MCTDH method for simulating medium/large systems. On the basis of a set of appropriate ML-trees, the UV absorption spectra for each electronic states are simulated, analyzed, and compared with the experimental spectra (only for the $\tilde{B} \leftarrow \tilde{X}$ band). The present ML-MCTDH results show that the ML-MCTDH calculations are accurate and the *ab initio* MMVCH model is suitable for ML-MCTDH calculations. In addition, the full dimensional *ab initio* quantum dynamical studies on formaldehyde oxide presented here complement the experimental observations.

Note added in proof: We discovered that the MCTDH calculations presented here are slowed down by the 3D mode combination (ν_4; ν_5; ν_7). After leaving ν_7 uncombined, the propagations became much faster. Now, ML-MCTDH and MCTDH calculations demand very similar CPU times.

[1] C. A. Taatjes, G. Meloni, T. M. Selby, A. J. Trevitt, D. L. Osborn, C. J. Percival, and D. E. Shallcross, J. Am. Chem. Soc. **130**, 11883–11885 (2008).

[2] O. Welz, J. D. Savee, D. L. Osborn, S. S. Vasu, C. J. Percival, D. E. Shallcross, and C. A. Taatjes, Science **335**, 204–207 (2012).

[3] D. Stone, M. Blitz, L. Daubney, T. Ingham, and P. Seakins, Phys. Chem. Chem. Phys. **15**, 19119–19124 (2013).

[4] H. Huang, A. J. Eskola, and C. A. Taatjes, J. Phys. Chem. Lett. **3**, 3399–3403 (2012).

[5]J. M. Beames, F. Liu, L. Lu, and M. I. Lester, J. Am. Chem. Soc. **134**, 20045–20048 (2012).

[6]E. P. F. Lee, D. K. W. Mok, D. E. Shallcross, C. J. Percival, D. L. Osborn, C. A. Taatjes, and J. M. Dyke, Chem. - Eur. J. **18**, 12411–12423 (2012).

[7]B. Ouyang, M. W. McLeod, R. L. Jones, and W. J. Bloss, Phys. Chem. Chem. Phys. **15**, 17070–17075 (2013).

[8]J. M. Beames, F. Liu, L. Lu, and M. I. Lester, J. Chem. Phys. **138**, 244307 (2013).

[9]J. H. Lehman, H. Li, J. M. Beames, and M. I. Lester, J. Chem. Phys. **139**, 141103 (2013).

[10]L. Sheps, J. Phys. Chem. Lett. **4**, 4201–4205 (2013).

[11]C. J. Percival, O. Welz, A. J. Eskola, J. D. Savee, D. L. Osborn, D. O. Topping, D. Lowe, S. R. Utembe, A. Bacak, G. McFiggans, M. C. Cooke, P. Xiao, A. T. Archibald, M. E. Jenkin, R. G. Derwent, I. Riipinen, D. W. K. Mok, E. P. F. Lee, J. M. Dyke, C. A. Taatjes, and D. E. Shallcross, Faraday Discuss. **165**, 45–73 (2013).

[12]M. Boy, D. Mogensen, S. Smolander, L. Zhou, T. Nieminen, P. Paasonen, C. Plass-Dülmer, M. Sipilä, T. Petäjä, L. Mauldin, H. Berresheim, and M. Kulmala, Atoms. Chem. Phys. **13**, 3865–3879 (2013).

[13]C. A. Taatjes, D. E. Shallcross, and C. J. Percival, Phys. Chem. Chem. Phys. **16**, 1704–1718 (2014).

[14]D. Stone, M. Blitz, L. Daubney, N. U. M. Howes, and P. Seakins, Phys. Chem. Chem. Phys. **16**, 1139–1149 (2014).

[15]Y.-T. Su, H.-Y. Lin, R. Putikam, H. Matsui, M. C. Lin, and Y.-P. Lee, Nat. Chem. **6**, 477–483 (2014).

[16]W.-L. Ting, Y.-H. Chen, W. Chao, M. C. Smith, and J. J.-M. Lin, Phys. Chem. Chem. Phys. **16**, 10438–10443 (2014).

[17]J. Li, S. Carter, J. M. Bowman, R. Dawes, D. Xie, and H. Guo, J. Phys. Chem. Lett. **5**, 2364–2369 (2014).

[18]Y.-T. Su, Y.-H. Huang, H. A. Witek, and Y.-P. Lee, Science **340**, 174–176 (2013).

[19]H.-D. Meyer, U. Manthe, and L. S. Cederbaum, Chem. Phys. Lett. **165**, 73–78 (1990).

[20]U. Manthe, H.-D. Meyer, and L. S. Cederbaum, J. Chem. Phys. **97**, 3199–3213 (1992).

[21]H.-D. Meyer, "Multiconfiguration time-dependent Hartree method," in *The Encyclopedia of Computational Chemistry*, edited by P. v. R. Schleyer, N. L. Allinger, T. Clark, J. Gasteiger, P. A. Kollman, H. F. Schaefer III, and P. R. Schreiner (John Wiley and Sons, Chichester, 1998), Vol. 5, pp. 3011–3018.

[22]M. H. Beck, A. Jäckle, G. A. Worth, and H.-D. Meyer, Phys. Rep. **324**, 1–105 (2000).

[23]H.-D. Meyer and G. A. Worth, Theor. Chem. Acc. **109**, 251–267 (2003).

[24]*Multidimensional Quantum Dynamics: MCTDH Theory and Applications*, edited by H.-D. Meyer, F. Gatti, and G. A. Worth (Wiley-VCH, Weinheim, 2009).

[25]H.-D. Meyer, WIREs Comput. Mol. Sci. **2**, 351 (2012).

[26]H. Wang and M. Thoss, J. Chem. Phys. **119**, 1289–1299 (2003).

[27]U. Manthe, J. Chem. Phys. **128**, 164116 (2008).

[28]O. Vendrell and H.-D. Meyer, J. Chem. Phys. **134**, 044135 (2011).

[29]P. J. Knowles and N. C. Handy, Chem. Phys. Lett. **111**, 315–321 (1984).

[30]H.-J. Werner and P. J. Knowles, J. Chem. Phys. **82**, 5053–5063 (1985).

[31]P. J. Knowles and H.-J. Werner, Chem. Phys. Lett. **115**, 259–267 (1985).

[32]H.-J. Werner and P. J. Knowles, J. Chem. Phys. **89**, 5803–5814 (1988).

[33]P. J. Knowles and H.-J. Werner, Chem. Phys. Lett. **145**, 514–522 (1988).

[34]P. J. Knowles and N. C. Handy, Comput. Phys. Commun. **54**, 75–83 (1989).

[35]P. J. Knowles and H.-J. Werner, Theor. Chem. Acc. **84**, 95–103 (1992).

[36]H. Köppel, W. Domcke, and L. S. Cederbaum, Adv. Chem. Phys. **57**, 59 (1984).

[37]H. Köppel and W. Domcke, "Vibronic dynamics in polyatomic molecules," in *Encyclopedia of Computational Chemistry*, edited by P. v. R. Schleyer, N. L. Allinger, T. Clark, J. Gasteiger, P. A. Kollman, H. F. Schaefer III, and P. R. Schreiner (John Wiley and Sons, New York, 1998), pp. 3166–3182.

[38]G. A. Worth, H.-D. Meyer, H. Köppel, and L. S. Cederbaum, Int. Rev. Phys. Chem. **27**, 569–606 (2008).

[39]H.-J. Werner, P. J. Knowles, G. Knizia, F. R. Manby, and M. Schütz, WIREs Comput. Mol. Sci. **2**, 242–253 (2012).

[40]H.-J. Werner, P. J. Knowles, G. Knizia, F. R. Manby, M. Schütz *et al.*, MOLPRO, version 2012.1, a package of *ab initio* programs, 2012, see http://www.molpro.net.

[41]T. H. Dunning, J. Chem. Phys. **90**, 1007–1023 (1989).

[42]R. A. Kendall, T. H. Dunning, and R. J. Harrison, J. Chem. Phys. **96**, 6796–6806 (1992).

[43]D. E. Woon and T. H. Dunning, J. Chem. Phys. **98**, 1358–1371 (1993).

[44]K. A. Peterson, D. A. Woon, and T. H. Dunning, J. Chem. Phys. **100**, 7410–7415 (1994).

[45]A. K. Wilson, T. v. Mourik, and T. H. Dunning, J. Mol. Struct. (THEOCHEM) **388**, 339–349 (1996).

[46]E. R. Davidson, Chem. Phys. Lett. **260**, 514–518 (1996).

[47]K. A. Peterson, R. A. Kendall, and T. H. Dunning, J. Chem. Phys. **99**, 1930–1944 (1993).

[48]R. Crehuet, J. M. Anglada, D. Cremer, and J. M. Bofill, J. Phys. Chem. A **106**, 3917–3929 (2002).

[49]G. A. Worth, M. H. Beck, A. Jäckle, and H.-D. Meyer, The MCTDH Package, Version 8.2, (2000); H.-D. Meyer, Version 8.3 (2002), Version 8.4 (2007); O. Vendrell and H.-D. Meyer, ML-MCTDH implemented in Version 8.5 (2011), see http://mctdh.uni-heidelberg.de/.

[50]J. C. Light, "Discrete variable representations in quantum dynamics," in *Time-Dependent Quantum Molecular Dynamics*, edited by J. Broeckhove and L. Lathouwers (Plenum, New York, 1992), pp. 185–199.

[51]J. C. Light and T. Carrington, Jr., Adv. Chem. Phys. **114**, 263–310 (2000).

[52]R. Schinke, *Photodissociation Dynamics* (Cambridge University Press, Cambridge, 1993).

[53]Q. Meng, S. Faraji, O. Vendrell, and H.-D. Meyer, J. Chem. Phys. **137**, 134302 (2012).

[54]Q. Meng and H.-D. Meyer, J. Chem. Phys. **138**, 014313 (2013).

[55]M. H. Beck and H.-D. Meyer, Z. Phys. D **42**, 113–129 (1997).

[56]D.-C. Fang and X.-Y. Fu, J. Phys. Chem. A **106**, 2988–2993 (2002).

[57]M. T. Nguyen, T. L. Nguyen, V. T. Ngan, and H. M. T. Nguyen, Chem. Phys. Lett. **448**, 183–188 (2007).

[58]See supplementary material at http://dx.doi.org/10.1063/1.4896201 for the one-dimensional functions of the dimensionless normal coordinates in the $\tilde{X}\,^1A'$, $\tilde{A}\,^1A''$, $\tilde{B}\,^1A'$, $\tilde{C}\,^1A'$, and $\tilde{D}\,^1A''$ states, and the comparisons between the MCTDH and ML-MCTDH spectra for the $\tilde{A}$, $\tilde{B}$, and $\tilde{C}\sim\tilde{D}$ bands.

[59]W. Chehade, B. Gür, P. Spietz, A. Vorshelov, A. Serdyuchenko, J. P. Burrows, and M. Weber, Atmos. Meas. Tech. **6**, 1623–1632 (2013).

[60]H.-B. Chang and M.-B. Huang, ChemPhysChem **10**, 582–589 (2009).